Giant anomalous Hall and anomalous Nernst conductivities in antiperovskites and their tunability via magnetic fields

Harish K. Singh,* Ilias Samathrakis, Chen Shen, and Hongbin Zhang†
Institute of Materials Science, Technical University Darmstadt, Otto-Berndt-Strasse 3, 64287 Darmstadt, Germany

(Received 3 September 2021; accepted 22 March 2022; published 7 April 2022)

The anomalous Hall conductivity (AHC) and anomalous Nernst conductivity (ANC) are two prominent transport phenomena in ferromagnetic materials of a topological nature. Based on first-principles calculations, we evaluate the AHC and ANC of 35 cubic ferromagnetic antiperovskites (APVs) and observe giant AHC and ANC as large as 1128 S/cm and 6.31 $AK^{-1}m^{-1}$ for Co_3LiN and Co_3PtN, respectively. Detailed analysis reveals that the origin of giant ANC can be attributed to the occurrence of Weyl nodes near the Fermi energy, as demonstrated for Co_3PtN. Interestingly, both the magnitude and sign of AHC and ANC can be tuned by changing the magnetization (**M**) directions, which could be applied to realize spin-caloritronics devices.

DOI: 10.1103/PhysRevMaterials.6.045402

I. INTRODUCTION

The anomalous Hall effect (AHE) is one of the emergent topological properties in ferromagnetic materials [1], driven by the broken time-reversal symmetry and spin-orbital coupling (SOC) [2]. Plenty of reported ferromagnetic materials exhibit large anomalous Hall conductivity (AHC), such as $CrPt_3$ (2040 S/cm) [3] and Co_2MnAl (1800 S/cm) [4]. Moreover, the quantum anomalous Hall effect is interesting for spintronic applications such as magnetic sensors, memory devices, and data processing [5–8]. Recently, it was demonstrated that the AHC hinges on the magnetization direction [9,10]. For example, the AHC of hexagonal close-packed (hcp) Co decreases from 481 to 116 S/cm as the magnetization direction changes from the *c*-axis (easy axis) to the *ab* plane, respectively [9]. Whereas for CoPt, both the AHC sign and magnitude were altered, the AHC changes from −119to 107 S/cm, switching magnetization from the [001] to [110] direction, indicating a change in the AHC sign [10]. From a symmetry point of view, the magnetic space group of the material is closely related to the magnetic spin directions, which leads to a change in band topology and hence likely a change in the magnitude and sign of AHC appear. In addition to being seen ferromagnetically, finite AHC has been recently observed in noncollinear antiferromagnets [11], emerging from their exotic antiferromagnetic (AFM) spin order (Γ_{4g}/Γ_{5g}) in cubic antiperovskites Cr_3XN (X = Ir and Pt) and Mn_3XN (X = Ag, Au, Co, Ga, Hg, In, Ir, Ni, Pd, Pt, Rh, and Zn) [12–18], cubic Mn_3X (Z = Ir, Pt, and Rh), and hexagonal Mn_3X (X = Ga, Ge, and Sn) [11,19–23].

More interestingly, the concomitant anomalous Nernst effect indicates that an electric current can be generated perpendicular to both the applied heat gradient and magnetization direction [24,25]. Recently, the energized field of spin-caloritronics focuseing on the correlation between spintronics and thermoelectrics in magnetic materials, has attracted considerable attention due to their potential application in thermoelectric devices [26–28]. In this context, Weyl semimetals are promising to induce a significant anomalous Nernst effect, owing to the occurrence of Weyl nodes near the Fermi energy [29–31]. For instance, a large anomalous Nernst conductivity (ANC) of 10.0 $AK^{-1}m^{-1}$ was reported for the Weyl semimetal $Co_3Sn_2S_2$, primarily originating from the large Berry curvature around the Weyl points near the Fermi-energy [29,32]. Note that the number of the Weyl nodes can be tailored by magnetization direction hence has a sizable impact on the electronic state's topological character [33,34], resulting in tuning the material's topological properties. Furthermore, the kagome lattice is one of the determinants to induce enhanced ANC [29,35]. From this perspective, antiperovskites are fascinating, hosting a kagome lattice in the (111) plane, and also the Weyl nodes can be tuned with applied biaxial strain as observed in noncollinear Mn_3PdN [13].

In this work, we systematically evaluated the AHC and ANC of 35 cubic APV compounds M_3XZ (Table I and Fig. 1), possessing the ferromagnetic ground state predicted in our recent study [13] and considered that the magnetic directions [001], [110], and [111] are appropriately inclusive. These three directions are the special crystalline axes that define the magnetocrystalline anisotropy for cubic ferromagnetic materials. All 35 APVs considered in this study fulfill thermodynamical, mechanical, and dynamical stability criteria, comprising 24 experimentally reported compounds and 11 APVs predicted from our high-throughput screening [36]. The APVs in a ferromagnetic state exhibit a large AHC and ANC, such as Co_3LiN attains an absolute AHC as large as 1128 S/cm, and Co_3PtN displays a giant ANC of 6.31 $AK^{-1}m^{-1}$, which is nearly the same as in cubic Fe_3Pt ferromagnetic (6.2 $AK^{-1}m^{-1}$) [37]. We investigated the Weyl points to identify the origin of large AHC and ANC, revealing the Weyl points' contribution to the total AHC and ANC. Next, we carried out a comparison of AHC and ANC

*harish@tmm.tu-darmstadt.de
†hzhang@tmm.tu-darmstadt.de

TABLE I. The compilation of MAE, AHC, and ANC of the APV compounds. The MAE is calculated using Eq. (4). The absolute AHC and ANC values are presented at the Fermi energy and the absolute values of AHC are obtained using equations $\sigma_{[001]} = \sigma_z$, $\sigma_{[110]} = \frac{1}{\sqrt{2}}(\sigma_x + \sigma_y)$, and $\sigma_{[111]} = \frac{1}{\sqrt{3}}(\sigma_x + \sigma_y + \sigma_z)$. The absolute values of ANC are obtained using equations $\alpha_{[001]} = \alpha_z$, $\alpha_{[110]} = \frac{1}{\sqrt{2}}(\alpha_x + \alpha_y)$, and $\alpha_{[111]} = \frac{1}{\sqrt{3}}(\alpha_x + \alpha_y + \alpha_z)$ and the ANC data are provided for 300 K. The AHC and ANC have not yet been measured experimentally for the ferromagnetic antiperovskites. The list of experimentally known antiperovskites for which the Curie temperature (T_c) is reported (last column). The energy-dependent AHCs and ANCs plots are provided in the Supplementary Material Figs. S3 and S4, respectively [82].

S.No.	M_3XZ Compounds	MAE (μeV/atom) [001–111]	[001–110]	[110–111]	AHC (S/cm) [001]	[110]	[111]	ANC (A/mK) [001]	[110]	[111]	T_c (K)
(1)	Co_3AuN	−4.4	−4.2	−0.2	480.2	534.9	548.5	0.97	−0.62	−0.33	
(2)	Co_3CdN	−0.2	0.8	−1.0	785.9	751.2	604.4	−3.27	−3.39	−3.90	
(3)	Co_3CuN	6.6	−0.8	7.4	349.3	570.8	593.1	2.84	3.31	2.33	650.0 [43]
(4)	Co_3GaN	−0.8	−1.4	0.6	559.2	529.2	536.2	−1.31	−1.31	−1.27	
(5)	Co_3GeC	−8.0	−11.4	3.4	72.9	129.0	152.8	−0.87	−1.35	−1.20	
(6)	Co_3GeN	−3.4	−2.8	−0.6	231.7	331.3	348.4	−1.26	−2.32	−3.33	
(7)	Co_3InN	−3.8	−5.0	1.2	482.6	474.8	470.0	−0.57	−0.08	−0.006	
(8)	Co_3LiN	12.0	−42.4	54.4	878.8	126.4	1127.6	−1.72	0.43	−3.03	
(9)	Co_3MgC	−1.2	−1.0	−0.2	283.4	288.8	−290.8	−0.57	−0.19	0.05	
(10)	Co_3PdN	−1.0	−2.6	1.6	158.6	190.6	241.6	0.90	0.46	0.25	
(11)	Co_3PtN	−41.6	−33.0	−8.6	710.4	558.4	755.4	6.31	4.41	3.81	
(12)	Co_3RhN	6.0	4.8	1.2	−116.1	243.7	258.7	−0.52	0.48	0.49	
(13)	Co_3SnC	1.2	25.2	−24.0	−51.7	166.3	22.3	−0.82	−1.13	−1.49	3.6 [44]
(14)	Co_3SnN	3.0	−19.0	22.0	−0.03	32.3	48.2	−2.62	−2.77	−2.39	
(15)	Co_3ZnC	−0.8	−0.6	−0.2	209.4	−280.7	266.4	−0.37	−0.002	0.17	
(16)	Co_3ZnN	0.8	4.6	−3.8	930.4	1039.7	1068.4	−3.24	−4.65	−4.97	
(17)	Fe_3AgN	−3.6	−5.0	1.4	189.4	364.9	283.1	1.12	2.17	2.38	
(18)	Fe_3AlC	1.0	0.6	0.4	−135.8	−0.94	33.7	−0.036	−0.021	−0.14	100.0 [45]
(19)	Fe_3AuN	−4.2	−1.0	−3.2	514.7	603.2	626.4	1.19	0.40	1.08	
(20)	Fe_3CuN	3.4	6.8	−3.4	630.1	852.7	883.0	−0.07	1.35	1.52	
(21)	Fe_3GaN	−1.8	−1.2	0.6	262.2	242.1	215.4	2.53	2.65	2.63	
(22)	Fe_3InN	1.0	0.8	0.2	491.1	411.9	376.3	0.34	0.48	0.92	662.0 [46]
(23)	Fe_3IrN	−59.8	−59.2	−1.6	852.0	719.3	888.1	−0.62	−2.17	−1.64	
(24)	Fe_3NiN	−1.2	0.2	−1.4	286.1	402.9	29.5	−0.01	−0.35	0.10	
(25)	Fe_3PdN	52.0	0.6	51.4	361.9	517.0	559.5	−0.22	−0.51	0.01	601.0 [47]
(26)	Fe_3PtN	−3.8	−0.8	−3.0	−401.6	−445.1	−510.2	1.28	0.60	0.91	
(27)	Fe_3RhN	−3.6	−0.4	−3.2	170.6	124.5	134.2	−1.40	−2.01	−2.77	505.0 [48]
(28)	Fe_3SnN	−2.4	−1.6	−0.8	123.9	161.8	185.1	−1.63	−0.92	−1.05	
(29)	Fe_3ZnC	0.4	−1.2	1.6	63.5	119.6	181.2	−0.81	−1.43	−0.77	200.0 [45]
(30)	Fe_3ZnN	−3.6	7.2	3.8	−94.2	−75.0	−14.4	−1.43	−0.50	0.15	762.0 [49]
(31)	Mn_3AlC	−0.4	1.2	−1.6	199.4	188.2	199.8	−0.51	−0.77	−0.84	287.0 [50]
(32)	Mn_3AlN	−2.8	−0.4	−2.4	51.4	72.0	68.9	−1.14	−1.06	−1.12	818.0 [51]
(33)	Mn_3InC	−8.6	−1.0	−7.6	434.9	287.9	235.6	1.97	1.77	1.52	272.0 [52]
(34)	Ni_3CuC	5.2	4.0	1.2	254.4	−251.6	257.7	1.08	−1.82	2.02	
(35)	Ni_3LiC	6.2	5.2	1.0	265.8	262.1	245.0	4.09	5.39	5.81	

between ferromagnetic and noncollinear APVs. Thus, we distinguished that the ferromagnetic APVs have larger AHC and ANC than the noncollinear APVs. Furthermore, we realized that the AHC and ANC strongly depend on the magnetization directions and can be tuned significantly by switching the magnetization direction. In this context, we presented a thermopile structure to explain the comprehensive interplay between electric current (**I**), thermal gradient (∇T), and magnetization (**M**) directions.

II. COMPUTATIONAL DETAILS

Our density functional theory (DFT) calculations are conducted using the projector augmented wave (PAW) method as implemented in the VASP code [38]. A generalized gradient approximation (GGA) is used within the parametrized form of Perdew-Burke-Ernzerhof (PBE) to treat the exchange-correlation functional [39]. The energy cutoff of 600 eV is used for the plane-wave basis set, and the spin-orbit coupling (SOC) is taken into account for each APV system. A uniform k-mesh of $17 \times 17 \times 17$ is employed for the Brillouin zone integrations within the Monkhorst-pack scheme. The partial occupancies of the electronic states are smeared by using the Methfessel-Paxton smearing width of 0.06 eV. The total energy convergence criterion is set to 10^{-07}. The optimized lattice constants are considered from our previous high-throughput study [36].

We used the WANNIER90 code to obtain the maximally localized Wannier functions and get the tight-binding model Hamiltonian [40]. In total, 80 maximally localized Wannier

functions were constructed for every APV system by projecting the s, p, and d orbitals of M and X atoms and the s and p orbitals for the N or C atom. The AHC was computed using the WANNIERTOOLS code [41]. A uniform k-mesh of $401 \times 401 \times 401$ was used for the Berry curvature integration [42]. The AHC was determined in conformity with the following equation:

$$\sigma_{\alpha\beta} = -\frac{e^2}{\hbar}\int \frac{d\mathbf{k}}{(2\pi)^3}\sum_n f[\epsilon(\mathbf{k}) - \mu]\Omega_{n,\alpha\beta}(\mathbf{k}), \quad (1)$$

$$\Omega_{n,\alpha\beta}(\mathbf{k}) = -2\mathrm{Im}\sum_{m\neq n}\frac{\langle\psi_{\mathbf{k}n}|v_\alpha|\psi_{\mathbf{k}m}\rangle\langle\psi_{\mathbf{k}m}|v_\beta|\psi_{\mathbf{k}n}\rangle}{[\epsilon_m(\mathbf{k}) - \epsilon_n(\mathbf{k})]^2}, \quad (2)$$

where e is the elementary charge, μ is the chemical potential, $\psi_{n/m}$ denotes the Bloch wave function with energy eigenvalue $\epsilon_{n/m}$, $v_{\alpha/\beta}$ is the velocity operator along the Cartesian α/β direction, and $f[\epsilon(\mathbf{k}) - \mu]$ is the Fermi-Dirac distribution function. Here, $\{\alpha, \beta\} = \{\mathrm{x,y,z}\}$ denote the Cartesian coordinates. The AHC and Berry curvature can be classified as pseudovectors and represented in their vector-form notations as $\sigma_{n,\alpha\beta} = [\sigma_{n,x}, \sigma_{n,y}, \sigma_{n,z}] = [\sigma_{n,yz}, \sigma_{n,zx}, \sigma_{n,xy}]$ and $\Omega_{n,\alpha\beta} = [\Omega_{n,x}, \Omega_{n,y}, \Omega_{n,z}] = [\Omega_{n,yz}, \Omega_{n,zx}, \Omega_{n,xy}]$, respectively. The ANC is computed using the in-house developed PYTHON code. The validation of the code is done by reproducing the ANC of Mn_3NiN a noncollinear APV [16] (Fig. S1 [82]). The ANC is determined using the following equation:

$$a_{xy} = -\frac{1}{e}\int d\epsilon \frac{\partial f}{\partial \mu}\sigma_{\alpha\beta}(\epsilon)\frac{\epsilon - \mu}{T}, \quad (3)$$

where T is the temperature, μ the Fermi level, and ϵ is the point of the energy grid.

III. RESULTS AND DISCUSSION

A. Magnetocrystalline anisotropy energy

Magnetocrystalline anisotropy energy (MAE) is expressed as the difference of the total energies for different magnetization directions, which yields

$$\mathrm{MAE} = E_{\mathbf{e}_1} - E_{\mathbf{e}_2}, \quad (4)$$

where $\mathbf{e}_1$ and $\mathbf{e}_2$ are chosen to be along the [001], [110], and [111] directions for the cubic APV compounds considered in this work. The resulting MAEs are shown in Table I. For cubic materials, it is well known that MAE is mostly about a few μeV/atom, e.g., the MAE of body-centered cubic (bcc) Fe is -0.4 μeV/atom favoring the [001] direction as an easy axis [53]. It is found that the MAEs of 28 out of 35 cubic APVs are lower than 10 μeV/atom (Table I). Nevertheless, considerable MAE is obtained for Co_3LiN, Co_3PtN, Co_3RhN, Fe_3IrN, and Fe_3PdN (Table I). For instance, Fe_3IrN exhibits a significant MAE as large as -59.8 μeV with an easy axis in the [001] direction.

The magnitude of MAEs can be understood based on the strength of the atomic SOC, as marked by the SOC energy (E_{SOC}) [54]. Taking Fe_3IrN as an example, (ΔE_{SOC}) between the [001] and [111] magnetization directions read

$$\Delta E_{\mathrm{SOC}} = E_{\mathrm{SOC}}[001] - E_{\mathrm{SOC}}[111], \quad (5)$$

with the resulting ΔE_{SOC} as large as -295.1 μeV/atom. This indicates that the magnetization along the [001] direction is favored. Further analysis on the atom-resolved contributions reveals that the Ir atoms have dominant contributions (-1442 μeV/atom) in comparison to that(-12.9 μeV/atom) of Fe atoms. This can be attributed to the enhanced strength of atomic SOC, i.e., $\xi_{5d}^{\mathrm{Ir}} \sim 457$ meV in comparison to $\xi_{3d}^{\mathrm{Fe}} \sim 54$ meV. The E_{SOC} analysis is consistent for all the APV systems and equally valid to characterize their preferred magnetization direction.

The magnetization direction can be manipulated by applying an external magnetic field [55,56]. The measurement of the planar Hall effect demonstrates that the transport properties can be modified by changing the magnetization directions, as elucidated for $Co_{60}Fe_{20}B_{20}$ [56]. Depending on the MAE's size, different magnitudes of magnetic fields are required. For cubic materials, the MAE is small, thus, the magnetization direction can be easily manipulated by applying external magnetic fields. In most APV systems, the MAE is only a few μeV/atom (0.2–10 μeV/atom), therefore, the magnetization direction can be smoothly aligned with the direction of the external magnetic field.

B. Symmetry analysis

Symmetry plays an essential role in determining the linear response properties, including AHC and ANC. The shape of the AHC/ANC tensor elements can be obtained from the magnetic space group, where the resulting symmetry operations can lead to a specific distribution of the Berry curvature in the **k**-space and hence vanishing/finite values for AHC/ANC. The resulting symmetry of the Berry curvature depends on the relative orientation between the Berry curvature component and the rotation axis or the mirror plane. For instance, the Berry curvature component perpendicular to the mirror plane remains unchanged when the mirror symmetry is applied. On the other hand, the Berry curvature component parallel to the mirror plane changes its sign after considering the symmetry. For the magnetization direction [001], the magnetic space group is 123.345 ($P4/mm'm'$) [57], it contains 16 symmetry operations. Half of the symmetry operations change the sign of the Berry curvature Ω_x and Ω_y, the other half do not change the sign of Ω_x and Ω_y, while Ω_z is invariant under each symmetry operation. As an example, discrete symmetry operations such as the mirror plane M_{001} or the two-fold rotation axis (2_{001}) change the sign of the Berry curvature Ω_x and Ω_y, but Ω_z is invariant, transforming the Berry curvature according to the following relations [2]:

$$\Omega_x(-k_x, -k_y, k_z) = -\Omega_x(k_x, k_y, k_z),$$
$$\Omega_y(-k_x, -k_y, k_z) = -\Omega_y(k_x, k_y, k_z),$$
$$\Omega_z(-k_x, -k_y, k_z) = \Omega_z(k_x, k_y, k_z).$$

Consequently, the σ_x and σ_y components vanish by integrating the Berry curvatures according to Eq. (1). The σ_z component, on the other hand, is invariant under both symmetry operations, giving rise to a finite AHC. This is confirmed by our explicit evaluation of AHC for Fe_3IrN as shown in Fig. S2 [82], with vanishing σ_x and σ_y but a σ_z as large as

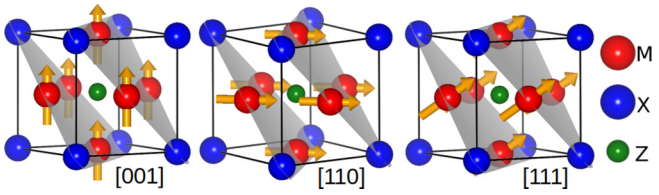

FIG. 1. The crystal structure of antiperovskites with chemical formula M_3XZ in $Pm\bar{3}m$ (221) space group, where M atoms are located at face-centers, whereas the X and Z atoms occupy the corner and body-centered position, respectively. The spin moments depict [001], [110], and [111] magnetization directions.

852 S/cm. For the magnetization direction [110], the magnetic space group is 65.486(Cmm'm$'$), which contains eight symmetry operations. For example, due to M'_{001} symmetry, $\Omega_z(-k_x, -k_y, k_z) = -\Omega_z(k_x, k_y, k_z)$ [2] leading to vanishing σ_z, while $\sigma_x = \sigma_y$ with nonzero values (Fig. S2) [82]. Finally, for the magnetization direction [111], the underlying symmetries of the magnetic space group $R-3m'$ (166.101) do not enforce a cancellation condition for any of the components of the Berry curvature; hence, they exhibit finite AHC (Fig. S2) [82], where $\sigma_x = \sigma_y = \sigma_z$. Therefore, considering AHC as a pseudovector $\sigma = \sigma_x \mathbf{e}_i + \sigma_y \mathbf{e}_j + \sigma_z \mathbf{e}_k$ (with $\mathbf{e}_{i/j/k}$ being the unit vectors along the Cartesian directions), it can be concluded that the AHC is always aligned with the magnetization direction for high-symmetric [001], [110], and [111] directions, as observed for tetragonal 3dPt alloys [10]. Hereafter, we adopt $\sigma_{[001]} = \sigma_z$, $\sigma_{[110]} = \frac{1}{\sqrt{2}}(\sigma_x + \sigma_y)$ and $\sigma_{[111]} = \frac{1}{\sqrt{3}}(\sigma_x + \sigma_y + \sigma_z)$, as summarized in Table I, where, the various components of AHC are defined as $\sigma_x = \sigma_{yz}$, $\sigma_y = \sigma_{zx}$, and $\sigma_z = \sigma_{xy}$. Such symmetry analysis applies to ANC as well. For instance, a possible thermopile structure mechanism summarizing the interplay between thermal gradient ($\nabla\mathbf{T}$), magnetization ($\mathbf{M}$), and electric current ($\mathbf{I}$) is depicted in Fig. 2. For an applied in-plane thermal gradient ($\nabla\mathbf{T_x}$) and out-of-plane magnetization $\mathbf{M}_z$, an electric current ($\mathbf{I_y}$) will generate along the y-direction [Fig. 2(a)], and for the out-of-plane thermal gradient ($\nabla\mathbf{T_z}$) and in-plane magnetization ($\mathbf{M}_x$) will also result in an electric current ($\mathbf{I_y}$) in the y-direction [Fig. 2(b)].

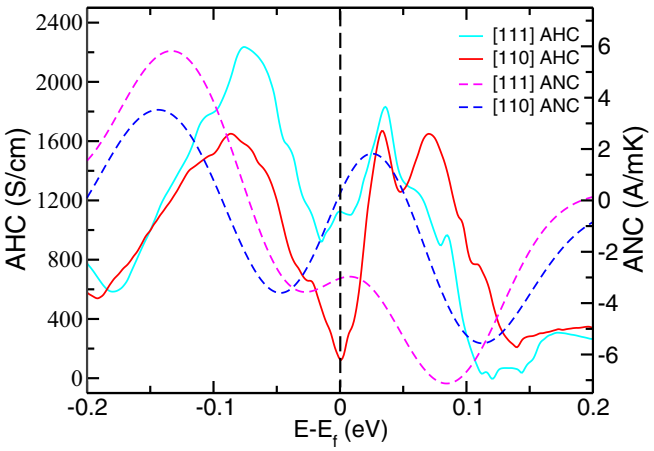

FIG. 3. The AHC and ANC of Co_3LiN for [111] and [110] magnetization directions, exhibiting the significant change in AHC and ANC on switching the magnetization direction from [111] to [110].

C. Large anomalous Hall conductivity

Table I displays the resulting AHC and ANC for the cubic APV compounds. The ferromagnetic cubic APVs can attain an AHC as large as 1000 S/cm. For instance, the magnitude of AHC for Co_3LiN and Co_3ZnN with magnetization aligned along the [111] direction is 1128 and 1068 S/cm, respectively. This is larger than that of bcc Fe (750 S/cm) [58,59] and nearly the same as that of the Weyl semimetal $Co_3Sn_2S_2$ (1130 S/cm) [29] and Fe_3Sn_2 (1100 S/cm) [60]. Moreover, the magnitude of AHC can be tuned significantly by changing the magnetization direction. For instance, the AHC of Co_3LiN changes from 1128 to 126 S/cm with the magnetization switched from the the [111] to [110] directions (Fig. 3). Furthermore, not only can the magnitude of AHC be tuned, but also its sign can be reversed by switching the magnetization directions. Taking an example of Co_3MgC, its AHC is 283 S/cm for the magnetization along the [001] direction, whereas it attains a negative value (−291 S/cm) for the [111] magnetization direction. The same is observed for Co_3RhN, Co_3SnC, Co_3ZnC, Fe_3AlC, and Ni_3CuC (Table I). Note that, for high-symmetry magnetization directions such as the [001], [110], and [111] directions considered in this work, both AHC and ANC are aligned along the direction of

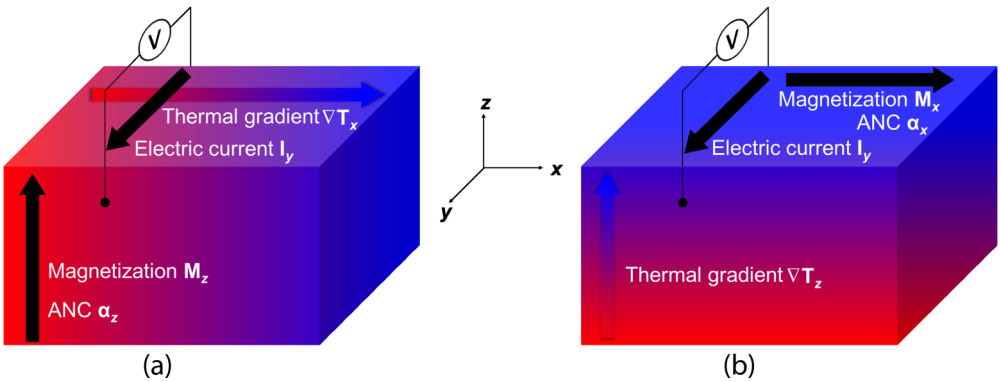

FIG. 2. Schematics illustration of thermopile structure for the (a) applied in-plane thermal gradient (∇T_x) and magnetization (M_z), generating an electric current in the y-direction and (b) exerted out-of-plane ∇T_z and M_x also lead to an electric current in the y-direction.

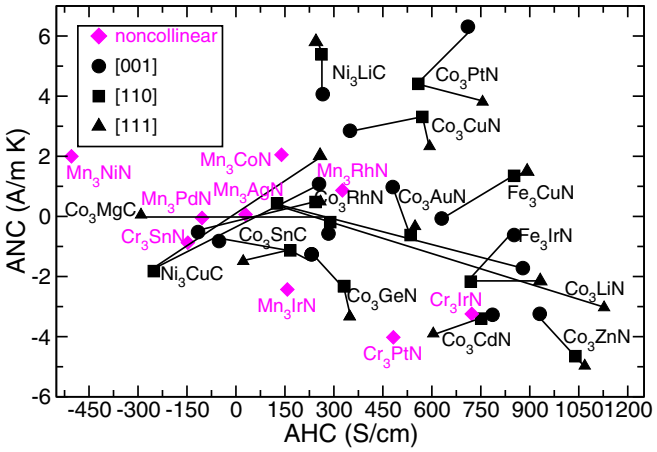

FIG. 4. The comparison of AHC and ANC for the ferromagnetic and noncollinear APV configurations. The solid line adjoins [001], [110], and [111] magnetization directions for the individual ferromagnetic APVs. The absolute values of AHC and ANC are illustrated at the Fermi energy and the ANC data are provided for 300 K. The direction of thermal gradient (∇T), magnetization (M), and electric current (I) for the plotted compounds are according to the mechanism explained in Fig. 2.

magnetization where a positive (negative) sign indicates that they are parallel (antiparallel) to the magnetization direction.

D. Comparison of AHC with noncollinear APVs

It is noted that the magnetic cubic APV compounds exhibit many interesting magnetic ground states. In our recent study [13] the total energies of eight magnetic configurations were evaluated and compared where 14 cubic APVs adopt the noncollinear configurations of the Γ_{4g}/Γ_{5g} types. The AHC/ANC vanishes for the Γ_{5g} state, whereas a finite AHC/ANC is expected for the Γ_{4g} state [18]. As shown in Fig. 4, the AHC of ferromagnetic APVs is, in general, larger than that of those with noncollinear configurations. As an illustration, the largest AHC of 1128 S/cm is obtained for Co_3LiN in ferromagnetic state, which is larger than the maximum AHC of 722 S/cm reported for noncollinear Cr_3IrN. In total, we found that six ferromagnetic APVs exceed the maximum AHC (722 S/cm) observed for the noncollinear state [13]. In Fig. 4, we compared the AHC/ANC of antiperovskites in their magnetic ground state. However, if we compare the AHC/ANC for the given ferromagnetic antiperovskite with the noncollinear state. In this case, it is not ensured to possess a higher AHC/ANC in the ferromagnetic state than the noncollinear state (Table S1) [82]. For instance, the AHC of Co_3PtN is larger in the noncollinear Γ_{4g} state (1465 S/cm) than the ferromagnetic [001] direction (710 S/cm). Additionally, it is noted that the APV compounds are closely connected to those with the Cu_3Au-type crystal structures [61]. It is observed that giant AHC can be obtained there as well, such as in Mn_3Ir (218 S/cm) [11] and Mn_3Pt (81 S/cm) [62].

E. Giant anomalous Nernst conductivity

Interestingly, it is observed that such cubic APV compounds exhibit giant ANCs, which obey the same symmetry arguments as AHC. Following the Mott formula [63], ANC is proportional to the energy derivative of AHC (the energy dependence of AHCs and ANCs are summarized in Figs, S3 and S4, respectively) and can be evaluated using Eq. (3). For ferromagnetic APVs, Co_3PtN exhibits ANC as large as 6.31 $AK^{-1}m^{-1}$ at 300 K for the [001] magnetization direction (Table I). This is quite comparable to that of Fe_3Pt (6.2 $AK^{-1}m^{-1}$) [37] and larger than the experimentally observed ANC in the ferromagnetic counterpart Co_2MnGa (4.0 $AK^{-1}m^{-1}$), Co_2FeGe (3.16 $AK^{-1}m^{-1}$), and Fe_3Ga (3.0 $AK^{-1}m^{-1}$) [30,64,65]. Furthermore, Ni_3LiC and Co_3ZnN also show a large ANC of 5.81 and −4.97 $AK^{-1}m^{-1}$ for the [111] magnetization direction, respectively. In total, seven APV systems attain an ANC larger than 3.0 $AK^{-1}m^{-1}$ at 300 K (Table I). Moreover, we found that the ANC of nine antiperovskites was reported in a recent study [37]. However, these nine reported antiperovskites excluded the antiperovskites that have a large ANC in our study (see Table S1 and the Supplementary Material [82]). In addition, to our knowledge, there is no AHC study reported for the ferromagnetic antiperovskites. Like AHC, ANC can also be tuned by switching the magnetization directions (Table I). For instance, the ANC of Co_3PtN alters from 6.31 $AK^{-1}m^{-1}$ to 3.81 $AK^{-1}m^{-1}$ as the magnetization direction changes from the [001] to [111] directions. Moreover, the sign of ANC could also change depending on the AHC slope's derivative $d\sigma_{xy}/d\epsilon$. For instance, the derivative of AHC for Co_3LiN changes from a positive (5318 S/cm.eV) value to a negative (−5190 S/cm.eV) one upon switching the magnetization direction from the [111] to [110] directions (Fig. 3). Correspondingly, the resulting ANC changes from −3.03 to 0.43 $AK^{-1}m^{-1}$.

For Fe_3ZnN, the sign and magnitude of ANC change from −1.43 to 0.15 $AK^{-1}m^{-1}$ upon switching out-of-plane magnetization from [001] to [111]. Therefore, for an applied magnetization $\mathbf{M}_z \parallel [001]/[111]$ and thermal gradient ∇T_x along the x-direction, an electric current will generate along $-y/y$ direction [Fig. 2(a)]. Similarly, for Co_3LiN, the sign of ANC changes from −1.72 to 0.43 $AK^{-1}m^{-1}$ for the magnetization $\mathbf{M}$ [100] to [110]. When magnetization $\mathbf{M}_x \parallel [100]/[110]$ is applied along the x-direction for the out-of-plane thermal gradient ∇T_z, an electric current will generate along the $-y/y$-direction [Fig. 2(b)]. Such an aspect is not only interesting in terms of the anisotropic nature of ANC, but also the Nernst voltage change in sign could possibly result in the generation of an in-plane thermal gradient ∇T caused by the rotation of the magnetization direction. For the Fe_4N antiperovskite, Isogami *et al.* showed that the Nernst voltage could be tuned significantly by altering the in-plane thermal gradient ∇T or magnetization $\mathbf{M}$ directions from [100] to [110] [66]. Usually, the anomalous Nernst effect is studied in the experiment for the out-of-plane thermal gradient ∇T and in-plane magnetization $\mathbf{M}$ [67,68] and also for the in-plane thermal gradient ∇T along with out-of-plane magnetization $\mathbf{M}$ [68,69]. However, the functional devices with the out-of-plane thermal gradient ∇T_z are more beneficial in the context of practical application for heat harvesting, as illustrated for the FePt thermopile with MgO(110) substrate [24,70,71].

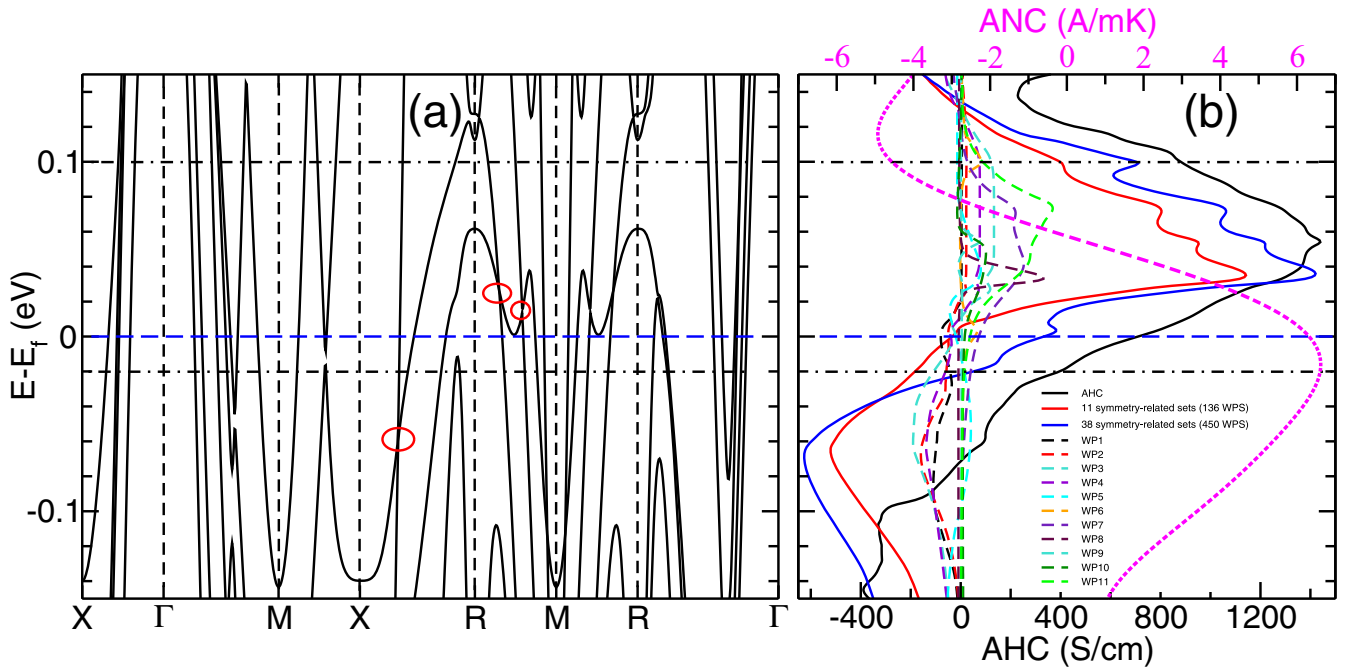

FIG. 5. For Co_3PtN, magnetization direction [001], the calculated (a) band structure is shown, where the red circles mark the band crossing between *R*-*M* and *X*-*R* and (b) the ANC is calculated at 300 K (magenta). The AHC is shown along with the analysis of the Weyl points. 11 (red) and 38 (blue) symmetry-related sets of Weyl points are the sum of the AHC of 136 Weyl points (WP1-11) and 450 Weyl points, respectively.

F. Comparison of ANC with noncollinear APVs

In comparison to the APVs with noncollinear magnetic ground states [13] the ANC of ferromagnetic APVs is more significant in most cases (Fig. 4). For instance, the largest ANC obtained in noncollinear Cr_3PtN is 4.02 $AK^{-1}m^{-1}$, which is less than Co_3PtN. Overall, 13 ferromagnetic APVs attain an ANC larger than 2.0 $AK^{-1}m^{-1}$. However, if we compare the ANC for the given ferromagnetic antiperovskite with the noncollinear state, the ANC of Cr_3IrN in the noncollinear Γ_{4g} is (−3.24 A/mK), which is higher than in the ferromagnetic [110] magnetization direction (1.66 A/mK) (Table S1) [82]. In terms of applications of such compounds as transversal thermoelectric materials, one apparent advantage is that the resulting ANC can be switched by controlling the magnetization directions, as we discussed above, which is not so convenient for APVs with noncollinear magnetic ground states.

G. Weyl point analysis

Turning now to the origin of giant ANC, it has been recently realized that the occurrence of Weyl nodes in the neighborhood of the Fermi-energy can contribute significantly to AHC and may lead to a singular-like behavior in AHC, thus a significant ANC [72–74]. This correlation between the large AHC/ANC and Weyl nodes around the Fermi energy was demonstrated in several recent studies [18,29,75,76]. For instance, in $Co_3Sn2_2S_2$, the Weyl nodes are located 60 meV above the Fermi energy, so there exists a large AHC peak at the Fermi energy, reaching a maximum value of 1100 S/cm [29]. Taking Co_3PtN with a giant ANC of 6.31 $AK^{-1}m^{-1}$ as an example, we carried out a detailed analysis of the electronic structure. As shown in Fig. 5(b), there exists a peak of AHC located about 54 meV above the Fermi energy. Correspondingly, there are two seemingly linear band crossings on the band structure, one above (∼ 20 meV) the Fermi-energy along *R*-*M* and the other below (∼ 50 meV) the Fermi-energy along *X*-*R* [Fig. 5(a)]. We investigated the Weyl points within the [−0.02, 0.1] eV energy window around the Fermi energy. We found 450 Weyl points which can be categorized into 38 symmetry-related Weyl points following the 16 symmetry operations associated with the $P4/mm'm'$ (123.345) magnetic space group. For the symmetry-associated Weyl point WP8 [Fig. 5(b)], the three-dimensional (3D) band structure is shown in Fig. 6, which consists of 16 symmetry-associated Weyl points at (0.499 −0.218 −0.492) and equivalent *k*-points with energy 25 meV

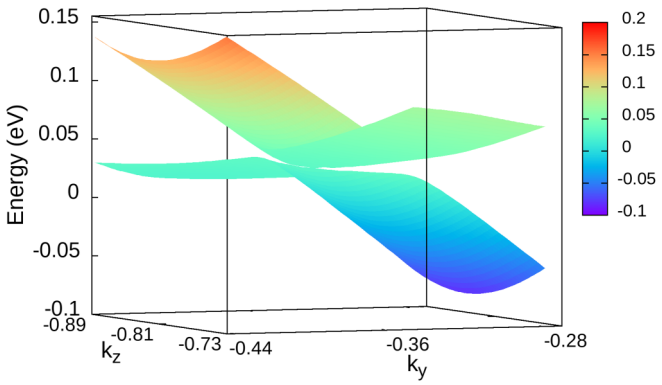

FIG. 6. The characterization of the Weyl points; the plots are in the (k_y, k_z) plane for the Weyl points (0.499 −0.218 −0.492) and the energy dispersion showing the degeneracies of the bands at the Weyl nodes.

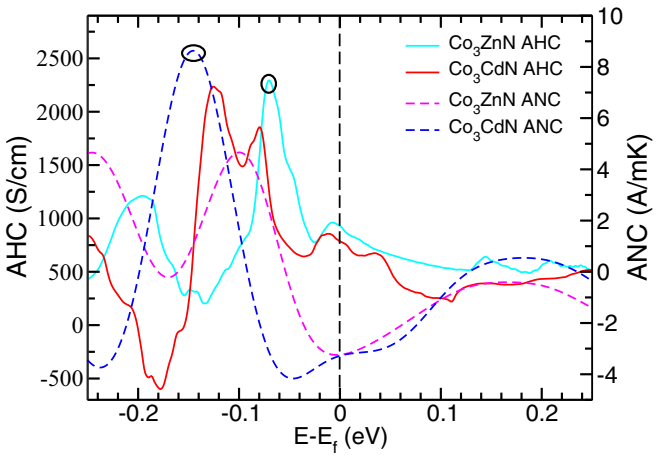

FIG. 7. The AHC and ANC of Co_3ZnN and Co_3CdN for the [001] magnetization direction. A large AHC and ANC peak is located at 70 and 147 meV below the Fermi energy, respectively.

above the Fermi energy. Subsequently, for each Weyl points (450), we evaluated the AHC by considering a small cube centering at spatial Weyl point position and with the acme of 0.08 (in the units of $2\pi/a$). Hence, we identified 11 sets of symmetry-related Weyl points (136) contributing primarily to the total AHC and reproducing the AHC peak above the Fermi energy [Fig. 5(b)]. However, the sum of AHC from 38 sets (450) of symmetry-related Weyl points is larger than the total AHC, demonstrating the significant contribution of Weyl points [Fig. 5(b)]. Therefore, it is suspected that the giant ANC can be attributed to the occurrence of Weyl nodes. It could be noticed from the Weyl points analysis of the Co3PtN that not all Weyl points contribute; 136 out of 450 Weyl points contribute primarily to the total AHC [Fig. 5(b)]. Hence, the occurrence of Weyl points does not necessarily give rise to a singular-like AHC. However, unlike $Co_3Sn_2S_2$, where there are three pairs of Weyl nodes located 60 meV above the Fermi energy, and one pair of Weyl node acts as a monopole sink and source of Berry curvature [29], whereas for Co_3PtN, there are many of them, which is a general feature of ferromagnetic materials [77]. Similarly, the AHC peaks for Co_3LiN and Co_3ZnN (Figs. 3 and 7) are also suspected to be resulting from the presence of Weyl nodes, but it is challenging to decompose the contribution because there are too many Weyl nodes.

H. Tuning AHC/ANC via chemical potential

Such singular behavior of AHC does not occur only in the proximity to the Fermi energy but also takes place at other energies. For instance, for the [001] magnetization direction, the AHC of Co_3ZnN can be tuned from 930 to 2249 S/cm by shifting the Fermi energy by 70 meV below the Fermi level (Fig. 7), with the ANC of 2.33 $AK^{-1}m^{-1}$. Similarly, the ANC can be tuned, as for the Co_3CdN, an extremely large ANC 8.62 $AK^{-1}m^{-1}$ could be obtained at 147 meV below the Fermi energy resulting due to the presence of a sharp AHC peak which reaches to maximum AHC (2235 S/cm) at 126 meV below the Fermi energy (Fig. 7). The Fermi level can be tuned by mechanical strain or doping, an effective method for optimising AHC, demonstrated in various magnetic materials [13,18,78–80]. For example, the AHC of $Co_3Sn_{2-x}In_xS_2$ is studied for various indium dopants [78]. Remarkably, the AHC at 2K increases to $\approx$ 2250 S/cm when $x = 0.15$, consisting of an intrinsic contribution plus a side-jump of $\approx$ 1500 S/cm and $\approx$ 750 S/cm due to skew-scattering, compared to an AHC value of $\approx$ 850 S/cm in the pristine $Co_3Sn_2S_2$. However, doping increases the extrinsic contribution to total AHC that arises from skew scattering and side-jump scattering [78,81]. Nevertheless, the intrinsic contribution plus side jump is twice as large as in the pristine case. In our study, for Co_3PtN, an AHC peak is located 54 meV above the Fermi energy. Based on the integration of the density of states, we find that doping of 0.3 electrons (for example, by Co $\rightarrow$ Ni doping at 10% as in $Co_{2.7}Ni_{0.3}PtN$) may shift the Fermi energy to the AHC peak.

The electronic band structure also changes due to mechanical strain. However, in the case where an AHC peak arises from the presence of Weyl points and these Weyl points shift to the Fermi energy under mechanical strain. In this case, the AHC peak is also shifted along the Weyl points and the dynamics of the Weyl points play a major role. As shown in Ref. [13], for the Mn_3PdN antiperovskite in the tetragonal phase, the Weyl points at 1% tensile strain shift from -31.82 meV to -0.29 meV near the Fermi energy at -1.2% compressive strain. As a result, the corresponding AHC peak is shifted, leading to an increase in AHC from -57.14 S/cm to -120 S/cm. Based on the above discussion, we therefore believe that the Fermi energy can be tuned up to 100 meV by doping or mechanical strain to achieve the expected results.

IV. CONCLUSION

In summary, we carried out a systematic evaluation of MAE, AHC, and ANC for 35 cubic APVs. As expected for cubic systems, the MAE is a few μeV/atom (0.2–10 μeV/atom) for most APV systems except in a few cases; hence their magnetization direction can be tuned easily. A giant AHC as large as 1000 S/cm is obtained in cubic APVs such as Co_3LiN and Co_3ZnN. Similarly, a giant ANC is observed for Co_3PtN and Ni_3LiC. Taking Co_3PtN as an example, we demonstrated that a large AHC/ANC is originated due to the presence of Weyl nodes close to the Fermi level, with dominant contributions to the total AHC/ANC. This indicates that AHC/ANC can be further tailored by shifting the Fermi energy via proper doping. In comparison to noncollinear APVs, the ferromagnetic APVs also exhibit larger AHC and ANC. Furthermore, we observed that the magnitude and sign of AHC/ANC could be tuned by switching the magnetization direction. Accordingly, we can adjust the thermal gradient (∇T) direction assisted by changing the magnetization directions. Therefore, it is imperative to perceive the importance of magnitude and sign change of ANC to realize ANC-based thermoelectric device applications. Moreover, the AHC and ANC have not yet been measured experimentally for any of the ferromagnetic antiperovskites. We hope that our work will incentivize the experimental efforts to corroborate our observations.

ACKNOWLEDGMENTS

The authors are grateful and acknowledge TU Darmstadt Lichtenberg's high-performance computer (HPC) support for the computational resources where the calculations were conducted for this project. The authors thank Dr. Benjamin Juhl from the TU Darmstadt HPC group for providing a special queue to perform the calculations. This project was supported by the Deutsche Forschungsgemeinschaft (DFG, German Research Foundation)-Project-ID 405553726-TRR 270.

[1] N. Nagaosa, J. Sinova, S. Onoda, A. H. MacDonald, and N. P. Ong, Anomalous hall effect, Rev. Mod. Phys. **82**, 1539 (2010).

[2] M.-T. Suzuki, T. Koretsune, M. Ochi, and R. Arita, Cluster multipole theory for anomalous hall effect in antiferromagnets, Phys. Rev. B **95**, 094406 (2017).

[3] A. Markou, J. Gayles, E. Derunova, P. Swekis, J. Noky, L. Zhang, M. N. Ali, Y. Sun, and C. Felser, Hard magnet topological semimetals in XPt_3 compounds with the harmony of berry curvature, Commun. Phys. **4**, 104 (2021).

[4] J. Kübler and C. Felser, Berry curvature and the anomalous hall effect in heusler compounds, Phys. Rev. B **85**, 012405 (2012).

[5] K. He, Y. Wang, and Q.-K. Xue, Topological materials: quantum anomalous hall system, Annu. Rev. Condens. Matter Phys. **9**, 329 (2018).

[6] M. Nadeem, A. R. Hamilton, M. S. Fuhrer, and X. Wang, Quantum anomalous hall effect in magnetic doped topological insulators and ferromagnetic spin-gapless semiconductors–a perspective review, Small **16**, 1904322 (2020).

[7] I. Žutić, J. Fabian, and S. D. Sarma, Spintronics: Fundamentals and applications, Rev. Mod. Phys. **76**, 323 (2004).

[8] A. Hirohata, K. Yamada, Y. Nakatani, I.-L. Prejbeanu, B. Diény, P. Pirro, and B. Hillebrands, Review on spintronics: Principles and device applications, J. Magn. Magn. Mater. **509**, 166711 (2020).

[9] E. Roman, Y. Mokrousov, and I. Souza, Orientation Dependence of the Intrinsic Anomalous Hall Effect in hcp Cobalt, Phys. Rev. Lett. **103**, 097203 (2009).

[10] H. Zhang, S. Blügel, and Y. Mokrousov, Anisotropic intrinsic anomalous hall effect in ordered 3d Pt alloys, Phys. Rev. B **84**, 024401 (2011).

[11] H. Chen, Q. Niu, and A. H. MacDonald, Anomalous Hall Effect Arising from Noncollinear Antiferromagnetism, Phys. Rev. Lett. **112**, 017205 (2014).

[12] Vu Thi Ngoc Huyen, M.-T. Suzuki, K. Yamauchi, and T. Oguchi, Topology analysis for anomalous hall effect in the noncollinear antiferromagnetic states of Mn_3AN (A= Ni, Cu, Zn, Ga, Ge, Pd, In, Sn, Ir, Pt), Phys. Rev. B **100**, 094426 (2019).

[13] H. K. Singh, I. Samathrakis, N. M. Fortunato, J. Zemen, C. Shen, O. Gutfleisch, and H. Zhang, Multifunctional antiperovskites driven by strong magnetostructural coupling, npj Comput. Mater. **7**, 98 (2021).

[14] D. Boldrin, I. Samathrakis, J. Zemen, A. Mihai, B. Zou, F. Johnson, B. D. Esser, D. W. McComb, P. K. Petrov, H. Zhang, and L. F. Cohen, Anomalous hall effect in noncollinear antiferromagnetic Mn_3NiN thin films, Phys. Rev. Material **3**, 094409 (2019).

[15] G. Gurung, D.-F. Shao, T. R. Paudel, and E. Y. Tsymbal, Anomalous hall conductivity of noncollinear magnetic antiperovskites, Phys. Rev. Material **3**, 044409 (2019).

[16] X. Zhou, J.-P. Hanke, W. Feng, S. Blügel, Y. Mokrousov, and Y. Yao, Giant anomalous nernst effect in noncollinear antiferromagnetic Mn-based antiperovskite nitrides, Phys. Rev. Material **4**, 024408 (2020).

[17] X. Zhou, J.-P. Hanke, W. Feng, F. Li, G.-Y. Guo, Y. Yao, S. Blügel, and Y. Mokrousov, Spin-order dependent anomalous hall effect and magneto-optical effect in the noncollinear antiferromagnets Mn_3XN with X= Ga, Zn, Ag, or Ni, Phys. Rev. B **99**, 104428 (2019).

[18] I. Samathrakis and H. Zhang, Tailoring the anomalous hall effect in the noncollinear antiperovskite Mn_3GaN, Phys. Rev. B **101**, 214423 (2020).

[19] G.-Y. Guo and T.-C. Wang, Large anomalous nernst and spin nernst effects in the noncollinear antiferromagnets Mn_3X (X= Sn, Ge, Ga), Phys. Rev. B **96**, 224415 (2017).

[20] J. Kübler and C. Felser, Non-collinear antiferromagnets and the anomalous hall effect, Europhys. Lett. **108**, 67001 (2014).

[21] A. K. Nayak, J. E. Fischer, Y. Sun, B. Yan, J. Karel, A. C. Komarek, C. Shekhar, N. Kumar, W. Schnelle, J. Kübler, C. Felser, and S. P. P. Parkin, Large anomalous hall effect driven by a nonvanishing berry curvature in the noncolinear antiferromagnet Mn_3Ge, Sci. Adv. **2**, e1501870 (2016).

[22] N. Kiyohara, T. Tomita, and S. Nakatsuji, Giant anomalous hall effect in the chiral antiferromagnet Mn_3Ge, Phys. Rev. Appl. **5**, 064009 (2016).

[23] Y. Zhang, Y. Sun, H. Yang, J. Železný, S. P. P. Parkin, C. Felser, and B. Yan, Strong anisotropic anomalous hall effect and spin hall effect in the chiral antiferromagnetic compounds Mn_3X (X= Ge, Sn, Ga, Ir, Rh, and Pt), Phys. Rev. B **95**, 075128 (2017).

[24] M. Mizuguchi and S. Nakatsuji, Energy-harvesting materials based on the anomalous nernst effect, Sci. Technol. Adv. Mat. **20**, 262 (2019).

[25] K. Behnia and H. Aubin, Nernst effect in metals and superconductors: a review of concepts and experiments, Rep. Prog. Phys. **79**, 046502 (2016).

[26] A. Slachter, F. L. Bakker, J.-P. Adam, and B. J. van Wees, Thermally driven spin injection from a ferromagnet into a nonmagnetic metal, Nat. Phys. **6**, 879 (2010).

[27] G. E. Bauer, E. Saitoh, and B. J. Van Wees, Spin caloritronics, Nat. Mater. **11**, 391 (2012).

[28] S. R. Boona, R. C. Myers, and J. P. Heremans, Spin caloritronics, Energy Environ. Sci. **7**, 885 (2014).

[29] E. Liu, Y. Sun, N. Kumar, L. Muechler, A. Sun, L. Jiao, S.-Y. Yang, D. Liu, A. Liang, Q. Xu *et al.*, Giant anomalous hall effect in a ferromagnetic kagome-lattice semimetal, Nat. Phys. **14**, 1125 (2018).

[30] A. Sakai, Y. P. Mizuta, A. A. Nugroho, R. Sihombing, T. Koretsune, M.-T. Suzuki, N. Takemori, R. Ishii, D. Nishio-Hamane, R. Arita *et al.*, Giant anomalous nernst effect and quantum-critical scaling in a ferromagnetic semimetal, Nat. Phys. **14**, 1119 (2018).

[31] Y. Xu, L. Das, J. Z. Ma, C. J. Yi, S. M. Nie, Y. G. Shi, A. Tiwari, S. S. Tsirkin, T. Neupert, M. Medarde, M. Shi, J. Chang, and T. Shang, Unconventional Transverse Transport Above and Below the Magnetic Transition Temperature in Weyl Semimetal $EuCd_2As_2$, Phys. Rev. Lett. **126**, 076602 (2021).

[32] H. Yang, W. You, J. Wang, J. Huang, C. Xi, X. Xu, C. Cao, M. Tian, Z.-A. Xu, J. Dai, and Y. Li, Giant anomalous nernst effect in the magnetic weyl semimetal $Co_3Sn_2S_2$, Phys. Rev. Material **4**, 024202 (2020).

[33] Z. Zhang, Q. Gao, C. C. Liu, H. Zhang, and Y. Yao, Magnetization-direction tunable nodal-line and weyl phases, Phys. Rev. B **98**, 121103(R) (2018).

[34] B. Zheng, B. Xia, R. Wang, J. Zhao, Z. Chen, Y. Zhao, and H. Xu, Tunable ferromagnetic weyl fermions from a hybrid nodal ring, npj Comput. Mater. **5**, 74 (2019).

[35] T. Asaba, V. Ivanov, S. Thomas, S. Savrasov, J. Thompson, E. Bauer, and F. Ronning, Colossal anomalous nernst effect in a correlated noncentrosymmetric kagome ferromagnet, Sci. Adv. **7**, eabf1467 (2021).

[36] H. K. Singh, Z. Zhang, I. Opahle, D. Ohmer, Y. Yao, and H. Zhang, High-throughput screening of magnetic antiperovskites, Chem. Mater. **30**, 6983 (2018).

[37] A. Sakai, S. Minami, T. Koretsune, T. Chen, T. Higo, Y. Wang, T. Nomoto, M. Hirayama, S. Miwa, D. Nishio-Hamane *et al.*, Iron-based binary ferromagnets for transverse thermoelectric conversion, Nature (London) **581**, 53 (2020).

[38] G. Kresse and J. Furthmüller, Efficient iterative schemes for ab initio total-energy calculations using a plane-wave basis set, Phys. Rev. B **54**, 11169 (1996).

[39] J. P. Perdew, K. Burke, and M. Ernzerhof, Generalized Gradient Approximation Made Simple, Phys. Rev. Lett. **77**, 3865 (1996).

[40] A. A. Mostofi, J. R. Yates, Y.-S. Lee, I. Souza, D. Vanderbilt, and N. Marzari, wannier90: A tool for obtaining maximally-localised wannier functions, Comput. Phys. Commun. **178**, 685 (2008).

[41] Q. Wu, S. Zhang, H.-F. Song, M. Troyer, and A. A. Soluyanov, Wanniertools : An open-source software package for novel topological materials, Comput. Phys. Commun. **224**, 405 (2018).

[42] D. Xiao, M.-C. Chang, and Q. Niu, Berry phase effects on electronic properties, Rev. Mod. Phys. **82**, 1959 (2010).

[43] Z. Hui, X. Tang, D. Shao, R. Wei, J. Yang, P. Tong, W. Song, X. Zhu, and Y. Sun, Self-assembled c-axis oriented antiperovskite soft-magnetic $CuNCo_3$ thin films by chemical solution deposition, J. Mater. Chem. C **3**, 4438 (2015).

[44] B. Wang, Y. Uwatoko, J. Cheng, and Y. Sun, Weak ferromagnetism and possible non-fermi-liquid behavior in the itinerant electronic material Co_3SnC, Phys. Rev. B **102**, 085153 (2020).

[45] F. Grandjean and A. Gerard, Study by mossbauer spectroscopy of the series of perovskite carbides $M_3M'C$ with M= Fe or Mn, and M'= Al, Ga, Ge, Zn, Sn, J. Phys. F: Met. Phys. **6**, 451 (1976).

[46] J. Burghaus, J. Kleemann, and R. Dronskowski, The ternary nitrides $InxFe_{4-x}N(0 < x < 0.8)$: Synthesis, magnetic properties, and theoretical considerations, Z. Anorg. Allg. Chem. **637**, 935 (2011).

[47] D. Music, J. Burghaus, T. Takahashi, R. Dronskowski, and J. Schneider, Thermal expansion and elasticity of $PdFe_3N$ within the quasiharmonic approximation, Eur. Phys. J. B **77**, 401 (2010).

[48] A. Houben, P. Müller, J. von Appen, H. Lueken, R. Niewa, and R. Dronskowski, Synthesis, crystal structure, and magnetic properties of the semihard itinerant ferromagnet $RhFe_3N$, Angew. Chem. Int. Ed. **44**, 7212 (2005).

[49] Y. Fu, S. Lin, and B. Wang, High-temperature soft magnetic properties of antiperovskite nitrides $ZnNFe_3$ and $AlNFe_3$, J. Magn. Magn. Mater. **378**, 54 (2015).

[50] B. Wang, J. Lin, P. Tong, L. Zhang, W. Lu, X. Zhu, Z. Yang, W. Song, J. Dai, and Y. Sun, Structural, magnetic, electrical transport properties, and reversible room-temperature magnetocaloric effect in antipervoskite compound $AlCMn_3$, J. Appl. Phys. **108**, 093925 (2010).

[51] J. Lin, B. Wang, P. Tong, W. Lu, L. Zhang, X. Zhu, Z. Yang, W. Song, J. Dai, and Y. Sun, AlN_xMn_3: A possible high-temperature soft magnetic material and strongly correlated system, Appl. Phys. Lett. **98**, 092507 (2011).

[52] T. Kanomata, T. Kaneko, and Y. Nakagawa, Magnetic properties of the intermetallic compound Mn_3InC, J. Solid State Chem. **96**, 451 (1992).

[53] S. V. Halilov, A. Y. Perlov, P. M. Oppeneer, A. N. Yaresko, and V. N. Antonov, Magnetocrystalline anisotropy energy in cubic Fe, Co, and Ni: Applicability of local-spin-density theory reexamined, Phys. Rev. B **57**, 9557 (1998).

[54] V. Antropov, L. Ke, and D. Åberg, Constituents of magnetic anisotropy and a screening of spin–orbit coupling in solids, Solid State Commun. **194**, 35 (2014).

[55] X. Liu, W. Lim, L. Titova, T. Wojtowicz, M. Kutrowski, K. Yee, M. Dobrowolska, J. Furdyna, S. Potashnik, M. Stone *et al.*, External control of the direction of magnetization in ferromagnetic InMnAs/GaSb heterostructures, Phys. E **20**, 370 (2004).

[56] K. M. Seemann, F. Freimuth, H. Zhang, S. Blügel, Y. Mokrousov, D. E. Bürgler, and C. M. Schneider, Origin of the Planar Hall Effect in Nanocrystalline $Co_{60}Fe_{20}B_{20}$, Phys. Rev. Lett. **107**, 086603 (2011).

[57] M. Seemann, D. Ködderitzsch, S. Wimmer, and H. Ebert, Symmetry-imposed shape of linear response tensors, Phys. Rev. B **92**, 155138 (2015).

[58] Y. Yao, L. Kleinman, A. H. MacDonald, J. Sinova, T. Jungwirth, D.-S. Wang, E. Wang, and Q. Niu, First Principles Calculation of Anomalous Hall Conductivity in Ferromagnetic bcc Fe, Phys. Rev. Lett. **92**, 037204 (2004).

[59] J. Weischenberg, F. Freimuth, J. Sinova, S. Blügel, and Y. Mokrousov, *Ab Initio* Theory of the Scattering-Independent Anomalous Hall Effect, Phys. Rev. Lett. **107**, 106601 (2011).

[60] L. Ye, M. Kang, J. Liu, F. Von Cube, C. R. Wicker, T. Suzuki, C. Jozwiak, A. Bostwick, E. Rotenberg, D. C. Bell *et al.*, Massive dirac fermions in a ferromagnetic kagome metal, Nature (London) **555**, 638 (2018).

[61] I. Opahle, H. K. Singh, J. Zemen, O. Gutfleisch, and H. Zhang, Effect of N, C, and B interstitials on the structural and magnetic properties of alloys with Cu_3Au structure, Phys. Rev. Research **2**, 023134 (2020).

[62] Z. Liu, H. Chen, J. Wang, J. Liu, K. Wang, Z. Feng, H. Yan, X. Wang, C. Jiang, J. Coey *et al.*, Electrical switching of the topological anomalous hall effect in a non-collinear antiferromagnet above room temperature, Nat. Electron. **1**, 172 (2018).

[63] D. Xiao, Y. Yao, Z. Fang, and Q. Niu, Berry-Phase Effect in Anomalous Thermoelectric Transport, Phys. Rev. Lett. **97**, 026603 (2006).

[64] S. N. Guin, K. Manna, J. Noky, S. J. Watzman, C. Fu, N. Kumar, W. Schnelle, C. Shekhar, Y. Sun, J. Gooth, and C. Felser, Anomalous Nernst effect beyond the magnetization scaling relation in the ferromagnetic heusler compound Co_2MnGa, NPG Asia Mater. **11**, 16 (2019).

[65] J. Noky, J. Gooth, C. Felser, and Y. Sun, Characterization of topological band structures away from the fermi level by the anomalous nernst effect, Phys. Rev. B **98**, 241106(R) (2018).

[66] S. Isogami, K. Takanashi, and M. Mizuguchi, Dependence of anomalous nernst effect on crystal orientation in highly ordered γ'-Fe_4N films with anti-perovskite structure, Appl. Phys. Express **10**, 073005 (2017).

[67] D. Meier, D. Reinhardt, M. Schmid, C. H. Back, J.-M. Schmalhorst, T. Kuschel, and G. Reiss, Influence of heat flow directions on nernst effects in Py/Pt bilayers, Phys. Rev. B **88**, 184425 (2013).

[68] T. Kikkawa, K. Uchida, S. Daimon, Y. Shiomi, H. Adachi, Z. Qiu, D. Hou, X.-F. Jin, S. Maekawa, and E. Saitoh, Separation of longitudinal spin seebeck effect from anomalous nernst effect: Determination of origin of transverse thermoelectric voltage in metal/insulator junctions, Phys. Rev. B **88**, 214403 (2013).

[69] S. Tu, J. Hu, G. Yu, H. Yu, C. Liu, F. Heimbach, X. Wang, J. Zhang, Y. Zhang, A. Hamzić *et al.*, Anomalous nernst effect in $Ir_2 2Mn_7 8/Co_2 0Fe_6 0B_2 0/MgO$ layers with perpendicular magnetic anisotropy, Appl. Phys. Lett. **111**, 222401 (2017).

[70] Y. Sakuraba, K. Hasegawa, M. Mizuguchi, T. Kubota, S. Mizukami, T. Miyazaki, and K. Takanashi, Anomalous nernst effect in L10-FePt/MnGa thermopiles for new thermoelectric applications, Appl. Phys. Express **6**, 033003 (2013).

[71] Y. Sakuraba, Potential of thermoelectric power generation using anomalous nernst effect in magnetic materials, Scr. Mater. **111**, 29 (2016).

[72] Q. Wang, Y. Xu, R. Lou, Z. Liu, M. Li, Y. Huang, D. Shen, H. Weng, S. Wang, and H. Lei, Large intrinsic anomalous hall effect in half-metallic ferromagnet $Co_3Sn_2S_2$ with magnetic weyl fermions, Nat. Commun. **9**, 3681 (2018).

[73] W. Shi, L. Muechler, K. Manna, Y. Zhang, K. Koepernik, R. Car, J. van den Brink, C. Felser, and Y. Sun, Prediction of a magnetic weyl semimetal without spin-orbit coupling and strong anomalous hall effect in the heusler compensated ferrimagnet Ti_2MnAl, Phys. Rev. B **97**, 060406(R) (2018).

[74] Y. Xu, L. Elcoro, Z.-D. Song, B. J. Wieder, M. Vergniory, N. Regnault, Y. Chen, C. Felser, and B. A. Bernevig, High-throughput calculations of magnetic topological materials, Nature (London) **586**, 702 (2020).

[75] M. P. Ghimire, J. I. Facio, J.-S. You, L. Ye, J. G. Checkelsky, S. Fang, E. Kaxiras, M. Richter, and J. van den Brink, Creating weyl nodes and controlling their energy by magnetization rotation, Phys. Rev. Research **1**, 032044(R) (2019).

[76] I. Samathrakis, T. Long, Z. Zhang, H. K. Singh, and H. Zhang, Enhanced anomalous nernst effects in ferromagnetic materials driven by weyl nodes, J. Phys. D **55**, 074003 (2022).

[77] D. Gosálbez-Martínez, I. Souza, and D. Vanderbilt, Chiral degeneracies and fermi-surface chern numbers in bcc fe, Phys. Rev. B **92**, 085138 (2015).

[78] H. Zhou, G. Chang, G. Wang, X. Gui, X. Xu, J.-X. Yin, Z. Guguchia, S. S. Zhang, T.-R. Chang, H. Lin, W. Xie, M. Z. Hasan, and S. Jia, Enhanced anomalous hall effect in the magnetic topological semimetal $Co_3Sn_{2-x}In_xS_2$, Phys. Rev. B **101**, 125121 (2020).

[79] K. S. Takahashi, M. Onoda, M. Kawasaki, N. Nagaosa, and Y. Tokura, Control of the Anomalous Hall Effect by Doping in $Eu_{1-x}La_xTiO_3$ Thin Films, Phys. Rev. Lett. **103**, 057204 (2009).

[80] R. Mathieu, A. Asamitsu, H. Yamada, K. S. Takahashi, M. Kawasaki, Z. Fang, N. Nagaosa, and Y. Tokura, Scaling of the Anomalous Hall Effect in $Sr_{1-x}Ca_xRuO_3$, Phys. Rev. Lett. **93**, 016602 (2004).

[81] H.-Y. Yang, B. Singh, B. Lu, C.-Y. Huang, F. Bahrami, W.-C. Chiu, D. Graf, S.-M. Huang, B. Wang, H. Lin *et al.*, Transition from intrinsic to extrinsic anomalous hall effect in the ferromagnetic weyl semimetal $PrAlGe_{1-x}Si_x$, APL Mater. **8**, 011111 (2020).

[82] Please see Supplementary Material at http://link.aps.org/supplemental/10.1103/PhysRevMaterials.6.045402 for the figures and tables with more information on this.